

Light intensity modulated photoluminescence for rapid series resistance mapping of perovskite solar cells

Kevin J. Rietwyk^{a,b,*}, Boer Tan^{a,b}, Adam Surmiak^{a,b}, Jianfeng Lu^{b,c}, David P. McMeekin^{a,b}, Sonia R. Raga^{a,b}, Noel Duffy^d, Udo Bach^{a,b}

^a Australian Research Council Centre of Excellence in Exciton Science, Department of Chemical Engineering, Monash University, Clayton, Victoria, 3800, Australia

^b Department of Chemical Engineering, Monash University, Clayton, Victoria, 3800, Australia

^c State Key Laboratory of Advanced Technology for Materials Synthesis and Processing, Wuhan University of Technology, Wuhan, 430070, China

^d CSIRO Energy Clayton Laboratories, Clayton, Victoria, 3168, Australia

ARTICLE INFO

Keywords:

Perovskite solar cells
Photoluminescence
Device characterization
Series resistance

ABSTRACT

The champion efficiency of small area perovskite solar cells is marginally behind their silicon counterpart. However, when up-scaled to large area modules, the performance of perovskite solar cells drops significantly due primarily to the inclusion of defects during fabrication. The future of perovskite solar cells depends greatly on the ability to fabricate high efficiency large area devices which requires methods for rapidly and reliably identifying the presence of damage or imperfections that limit their performance. In this work we employ, for the first time, intensity modulated photoluminescence to spatially map the series resistance of perovskite solar cells with high spatial resolution. The technique permits the rapid identification of a range of different macroscopic defects and quantifies the impact on the local series resistance. It is performed under steady-state conditions to avoid complications of transient behaviour occurring in the perovskite film. The robustness of the approach is demonstrated by characterising an entire batch of perovskite solar cells with the mean series resistance values validated using established electrical analysis methods. Our method can be readily applied by other research groups for device optimisation or scaled to large areas for automated process control and validation.

1. Introduction

Hybrid perovskite based solar cells (PSCs) have recently attained a certified power conversion efficiency (PCE) of 25.2%, less than 1% behind silicon single crystal [1], despite the first publication for photovoltaic applications only appearing in 2009 with an initial PCE of ~4% [2,3]. The rapid improvement in efficiency over the past decade can be attributed to optimisation of the chemical composition of the perovskite active layer, selective transport materials and interfaces. However, the future of perovskite based solar cells depends greatly on the ability to upscale the devices to full module size >800 cm² and while retaining high efficiencies [3–5]. The current record in PSC module (area 802 cm²) efficiency is just 11.6% [6]. The efficiency of solar cells tends to reduce with increased area due to the higher fault content compared to small research scale devices. A tool to spatially map these defected regions is key for optimisation of large area fabrication processes. To be effective, it must be straightforward and swift to perform

while catering to the notorious transient effects observed in perovskite devices that greatly complicate analysis.

Camera-based luminescence imaging techniques based on both photoluminescence (PL) and electroluminescence (EL) has proven to be effective for the characterisation of silicon and thin film photovoltaic devices at a research level and for in-line manufacturing [7–19]. In general these methods are fast, reliable, quantitative and non-destructive [10], can be applied to individual films/wafers, stacks of layers or complete devices and are applicable from macro to micro length scales [20]. There has been growing interest in applying these techniques to neat perovskite films and to date, luminescence imaging has been used to correlate the open circuit voltage to map the quantum yield and radiative recombination losses [21–24], the chemical composition [21,25], and interfacial recombination [24]. Meanwhile, such studies on perovskite photovoltaics have provided spatial information on long-term stability [26,27], film uniformity [28], current transport efficiencies [29], optical band gaps [30] and series resistance

* Corresponding author. Australian Research Council Centre of Excellence in Exciton Science, Department of Chemical Engineering, Monash University, Clayton, Victoria, 3800, Australia.

E-mail address: kevin.rietwyk@monash.edu (K.J. Rietwyk).

<https://doi.org/10.1016/j.nanoen.2020.104755>

Received 4 February 2020; Received in revised form 16 March 2020; Accepted 24 March 2020

Available online 1 April 2020

2211-2855/Crown Copyright © 2020 Published by Elsevier Ltd. All rights reserved.

[31].

Despite the wide breadth of luminescence imaging methods suitable for characterising perovskite materials/devices all of these techniques all have one thing in common, they rely on steady-state analysis. A number of reports have shown that the temporal effects that plague the electronic properties also affect the luminescence emission of perovskite films/devices in an unpredictable fashion, complicating quantitative analysis [32]. To perform detailed analysis it is often necessary to adjust the steady state condition by varying the light intensity and/or current/voltage (in the case of devices), waiting at each step for the system to stabilise before performing a measurement, adding up to hours to the total analysis time. Shifting the measurement to the frequency domain provides an elegant solution that reduces the time spent waiting for stability and enables the development of new modulation/perturbation capabilities.

In this work we show, for the first time, intensity modulated photoluminescence mapping (IMPL-Map) technique to spatially resolve the physical properties of photovoltaic devices. For this method, once the photovoltaic device has reached a steady-state condition, the light intensity is modulated to induce a likewise modulation in the luminescence intensity. The small light perturbation ensures linearity in the PL response enabling much faster reading of the device properties at multiple illumination conditions, in contrast to conventional analysis [12, 13, 31]. We have developed an analysis protocol for series resistance mapping based on IMPL-Map combined with a dynamic J-V scan and apply it to an entire batch of perovskite solar cells (normal) and three cells with an inverted structure (inverted). We provide evidence that our method is suitable for routine analysis of typical research devices. Demonstrated herein by devices with an average PCE of 16%, high resistance $\sim 10 \Omega \text{ cm}^2$ and notable hysteresis. The accuracy of the spatially-resolved series resistances is cross validated with a parallel calculation of the overall series resistance using the intensity-modulated current and voltage, simultaneously collected with the IMPL-Map. Moreover, we will discuss the conditions in which the method shows higher accuracy in the reading as well as the limitations observed at high and low voltages.

2. Background theory

Before detailing our approach we will provide a brief introduction to underlying assumptions used for our series resistance mapping method and commonly employed in this field, [7, 13–19]. To achieve the spatial information it is beneficial to treat the photovoltaic device as a 2D network of parallel nodes with the node size determined by the resolution of the camera. Each node contains a local photocurrent source J_L (assumed to be uniform across the device), a diode to model the radiative recombination and a series resistance $R_{S,i}$ to common terminals, as depicted in Fig. 1. To correlate the local voltage V_i with the luminescence intensity we will use the following relationship

$$\phi_i = C_i \exp\left(\frac{qV_i}{k_B T}\right) + B_i J_{L,i} \quad (1)$$

Where C_i and B_i are calibration constants, respectively and q , k_B and T have their usual meaning of the elementary charge, Boltzmann constant and temperature, respectively. The first term on the right hand side, relates the luminescence intensity to the local voltage. The term $B_i J_{L,i}$ originates from diffusion limited carriers, i.e. the illumination intensity dependent background. A simple correction can be applied by subtracting the luminescence measured at reverse bias $V_{Term} = -0.5 \text{ V}$ for each illumination intensity. For the rest of the paper we will only refer to the background corrected PL intensity

$$\phi_i^* = C_i \exp\left(\frac{qV_i}{k_B T}\right) \quad (2)$$

The difference between the local diode voltage V_i and the terminal

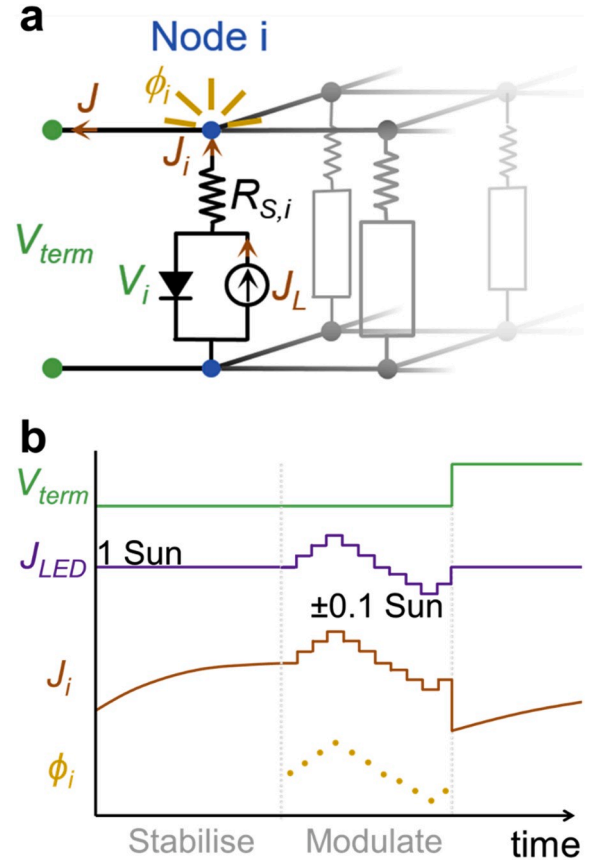


Fig. 1. a) Equivalent circuit of node i shown in a 2D network of parallel nodes that comprise a complete solar cell. Each node consists of a current source J_L (with a common value), diode with local voltage V_i and resistor $R_{S,i}$ contributing a current density of J_i to the total current of the device $J = \sum J_i$ and emitting some luminescence ϕ_i . b) Scheme of the IMPL measurement protocol showing that the device is held at a defined terminal voltage V_{Term} , at 1 Sun equivalent until the total current stabilises and the light intensity is modulated ± 0.1 Sun equivalent with concurrent measurements on the PL intensity ϕ_i . The terminal voltage is varied and the process is repeated.

voltage V_{Term} is the voltage drop across the local series resistance $R_{S,i}$ due to a local current density J_i , i.e. $V_i - V_{Term} = J_i R_{S,i}$. The local series resistance reflects the resistance to charge carrier transport between the space charge region in the absorber layer and the electrical contacts. In perovskite solar cells the series resistance is the combined resistance of electron and hole transport layers and the contacts, including the corresponding interfaces. Through Eq. (2), this relation provides a useful link between the terminal voltage, luminescence and the series resistance, however the quantity J_i is difficult to ascertain. Fortunately, as established by Kampwerth et al. [13] if the device is measured at two different operational conditions i.e. different light intensities and terminal voltages, but exhibits the same local luminescence ($dV_i = 0$), the recombination current must be equivalent and changes in the current density are due to the photocurrent $\Delta J_L = \Delta J_i$. The series resistance is given by

$$R_{S,i} = - \left. \frac{\Delta V_{Term}}{\Delta J_L} \right|_{dV_i=0} \quad (3)$$

In the original work, Kampwerth et al. [13] used a total of six images at various voltages and two light intensities to determine a series resistance map of a silicon solar cell. More recently, Walter et al. [31] used dynamic J-V scans at 4 different light intensities and proved that by waiting for the current to stabilise at each operational condition, prior to measuring the PL, the series resistance could be mapped across

perovskite solar cells. While an important step forward for characterising PSC, the approach was only demonstrated for two devices, with 4 maps each across a very narrow range of voltages (~ 0.1 V). To overcome these shortcomings (limited voltage range and excessively long measurements times) we have devised a method based on a light modulation at each voltage during a single dynamic J-V scan, we can obtain a resistance map for each voltage, above ~ 0.7 V across a range of >0.2 V, in approximately half the amount of time.

3. Results and discussion

An overview of the measurement procedure employed in this work is shown as a scheme for a single voltage step in Fig. 1b with an example of the experimentally measured current throughout the course of a complete dynamic JV scan provided in Fig. 2a. We performed a dynamic JV scan starting at $V_{Term} = -0.5$ V and incrementally raised the voltage to open circuit or slightly beyond. At each voltage the current was monitored and once it had stabilised, i.e. the rate of change was below a threshold 10^{-6} A/s or 0.1%/s, the light intensity was modulated. A small perturbation of 1 ± 0.1 Suns was used as this range has proven suitable

for IMVS studies [33–35] of PSCs and it is sufficiently small to ensure that the resulting change in PL can be approximated as linear. The PL was captured during a piecewise sinusoidal modulation as shown in the inset of Fig. 2a in order to ensure the light intensity for each image is well-known. For two cells (F and H) instead of a fixed rate modulation, the current was allowed to stabilise at each light intensity, similar to approach employed by Walter et al. [31], as discussed later in the paper. The short circuit J_{SC} is used to determine the photocurrent J_L at each light intensity. Fig. 2d shows that the variation in the PL correlates with changes in the light intensity and can be fitted with a simple sinusoidal function. Stabilised currents measured at each light intensity, for each voltage, are used to reproduce JV scans, as shown in Fig. 2b. Fig. 2c shows the PL intensity plotted against the time, with increasing voltage from left to right with the light modulation after stabilisation clearly visible at each voltage.

The analysis on the experimental data to determine both the local $R_{S,i}$ and global $R_{S,JV}$ series resistances is outlined in Fig. 3. In the case of the former, we employ the same basic concept of Kampwerth et al. [13] and solve equation (3) but using various light intensities at each voltage rather than multiple voltages at only two light intensities. The core

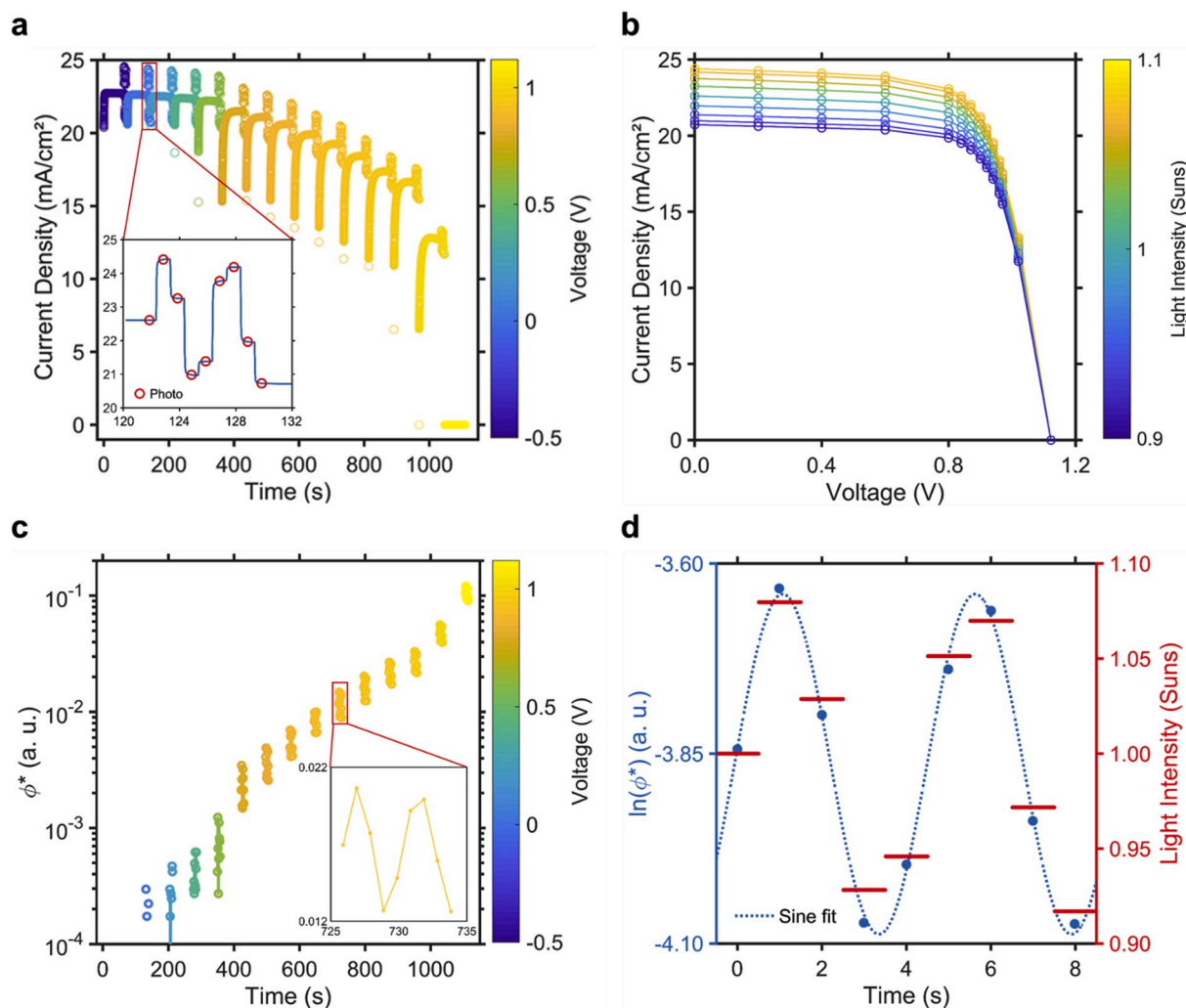


Fig. 2. a) Current density against time with variation in the voltage indicated via the colour bar. At each voltage the current was measured until it stabilised and a light modulation was performed. The inset shows the variation in the current density at J_{SC} due to the light modulation, after which the intensity is returned to 1 Sun. These values were used to determine the photocurrent at each light intensity with circles denoting when images were taken to determine the photoluminescence. b) Steady state J-V curves from the data in a) with the light intensities varying from 0.9 to 1.1 Suns, as indicated in the colour bar. A truncated set of data points were measured to reduce the duration and minimise the likelihood of degradation. c) PL intensities for a single pixel (background-corrected) plotted against time at the corresponding voltage. The inset shows the modulation of the PL intensity for one set of modulations. d) $\ln(\phi^*)$ (left axis) and light intensity (right axis) vs. time t during a light modulation, with a sine fit $\ln(\phi^*) = a + b \sin(c + dt)$, where a-d are fitting parameters.

requirement for this analysis is that the local voltage V_i remains constant, as evidenced by constant PL intensity at each pixel, under different operating conditions i.e. $dV_i = k_B T/q \ln(\phi^*) = 0$. This has been plotted against the photocurrent for selection of voltages in Fig. 3a. For each voltage we fit the data using two approaches, a sine and a linear fitting method. For the former, we fit the light intensity and photoluminescence with time t using a simple sinusoidal function $X = a + b \sin(c + dt)$, where $X = kT/q \ln(\phi^*)$ and J_L and a, b, c and d are fitting parameters. Since the periods of the modulation of J_L and PL should be identical, a common value of d is used for both. To determine dV_i from the sine fits, we discard the phase information and linearise the fits by using the offsets and amplitudes (a and b values) in order to permit a simple extrapolation. The linear fits, are simple linear regressions of the data as presented in Fig. 3a. It is worth noting that typically there is excellent agreement between the two fitting approaches. As a proof-of-concept we will focus on the sine fitting approach for the rest of the paper; although the direct linear regression is faster to calculate (minutes compared to tens of minutes), except for cells F and H where a sine fit is not possible. To determine the series resistance we must identify the PL intensities common for two voltages, which is illustrated as a horizontal line ($dV_i = 0$) that bisects two regressions, see Fig. 3b. The corresponding photocurrent and terminal voltage values are used to calculate the series resistance using equation (3).

In order to validate the local series resistance measurements we have devised a method to calculate the aggregated or global resistance $R_{S,JV}$ of the complete cell from the JV data presented in Fig. 2. The mean of the

local series resistance $\langle R_{S,i} \rangle$ has been shown to give good agreement with $R_{S,JV}$ in the literature [12,31,38] and by using the J-V data there is an inherent consistency between the resistances while preventing the need for further measurements. Our approach is a variant of the well-established double or multiple light method (MLM) [31,36,37], based on the single diode equation and treating the complete cell as a single node with an equivalent circuit as shown in Fig. 1a,

$$J = J_L - J_0 \left(\exp\left(\frac{q(V_{Term} + JR_{S,JV})}{nK_B T}\right) - 1 \right) \quad (4)$$

where n is the ideality constant and J_0 is the dark saturation current. It is reasonable to assume that $\exp\left(\frac{q(V_{Term} + JR_{S,JV})}{nK_B T}\right) \gg 1$ removing the J_0 term and that n, J_0 and $R_{S,JV}$ are invariant with the light intensities used here. Thus Eq. (4) can be rewritten as follows,

$$\ln\left(\frac{J_L - J}{J_0}\right) = \frac{q(V_{Term} + JR_{S,JV})}{nK_B T} \quad (5)$$

If when varying the light intensity, the condition $d \ln(J_L - J) = 0$ is satisfied then the equation can be rearranged to give the global resistance,

$$R_{S,JV} = - \left. \frac{\Delta V_{Term}}{\Delta J} \right|_{d \ln(J_L - J) = 0} \quad (6)$$

In this work we exploit this relationship by plotting $\ln(J_L - J)$ against J ,

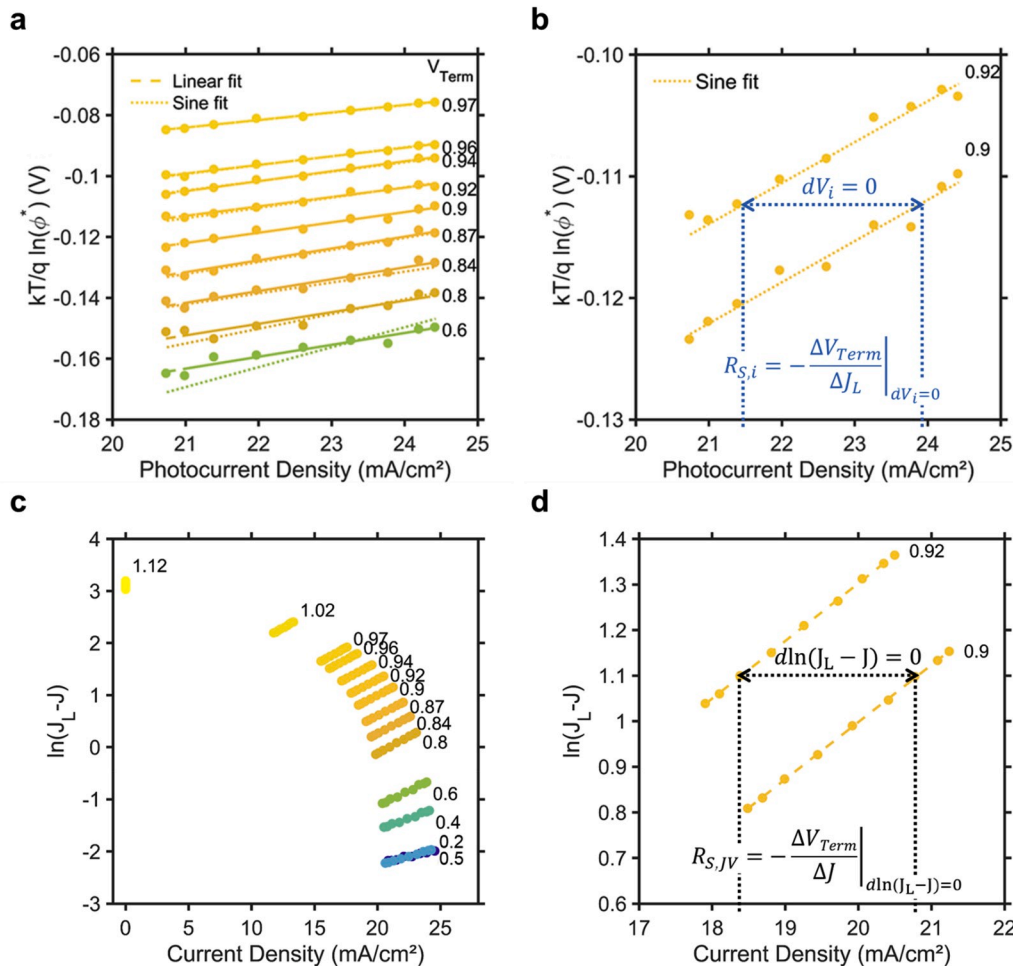


Fig. 3. a) Example plot of $kT/q \ln(\phi^*)$ vs. photocurrent density J_L at V_{Term} values indicated, for one pixel. b) The data in a) rescaled to illustrate the determination of the local series resistance $R_{S,i}$. c) Plot $\ln(J_L - J)$ against the stabilised current density J measured at the voltages given in the plot with different light intensities. d) The data from c) rescaled to illustrate the determination of the global series resistance $R_{S,JV}$ in accordance with the MLM method.

for the values measured during the modulation for each voltage (Fig. 3c). From this point, the global resistance is calculated in an analogous fashion to the local resistance, as illustrated in Fig. 3d. The data is fitted using linear regressions for each terminal voltage. Between two voltages $d\ln(J_L - J) = 0$ is identified by using a horizontal line that bisects two regressions with extrapolation of the fits applied if necessary. The key advantage of this method is that it provides an J-V based series resistance to validate our PL determined resistance within the same set of data and at the same voltages, providing a direct comparison. A short analysis on the impact of series resistance on the operation and performance of solar cells is provided in the supplementary information.

To demonstrate the effectiveness of our series resistance mapping technique we have performed the analysis across an entire batch of perovskite solar cells; a selection is presented in Fig. 4 while the remainder are provided in the supplementary information. In Fig. 4, from left to right, for cells B, E and C, we present maps of the PL intensity and series resistance $R_{S,i}$ measured at $V_{Term} = \sim V_{MPP}$ (maximum power point voltage) and plot of $\langle R_{S,i} \rangle$ and $R_{S,JV}$ for a range of voltages. It is

interesting to note, that despite the cells presented having been fabricated with a single batch (by a single researcher, using the same set of precursor solutions and film growth procedures) there are considerable differences in the PL and $R_{S,i}$ maps. This highlights the high variability of the selective contacts and the microstructure of perovskite films in PSCs.

For each cell there is a random distribution of features including lines, small irregularly shaped patches and highly symmetrical or circular regions. Patterns of lines that spread radially from a single point were attributed to spin-coating. Both the PL and $R_{S,i}$ maps show this pattern for the cells which has been observed previously in luminescence measurements on perovskite solar cells and are attributed to the TiO_2 mesoporous scaffold [20,31]. Curved lines are most likely scratches within one of the various layers, which typically raise the series resistance with fine examples towards the top of cells B and E. The irregular patches may be caused by dust or other small particles sitting on the surface during fabrication, localised delamination of the perovskite layer from the selective contacts or localised damage. Circular shaped patches can arise from a number of different factors including droplets of

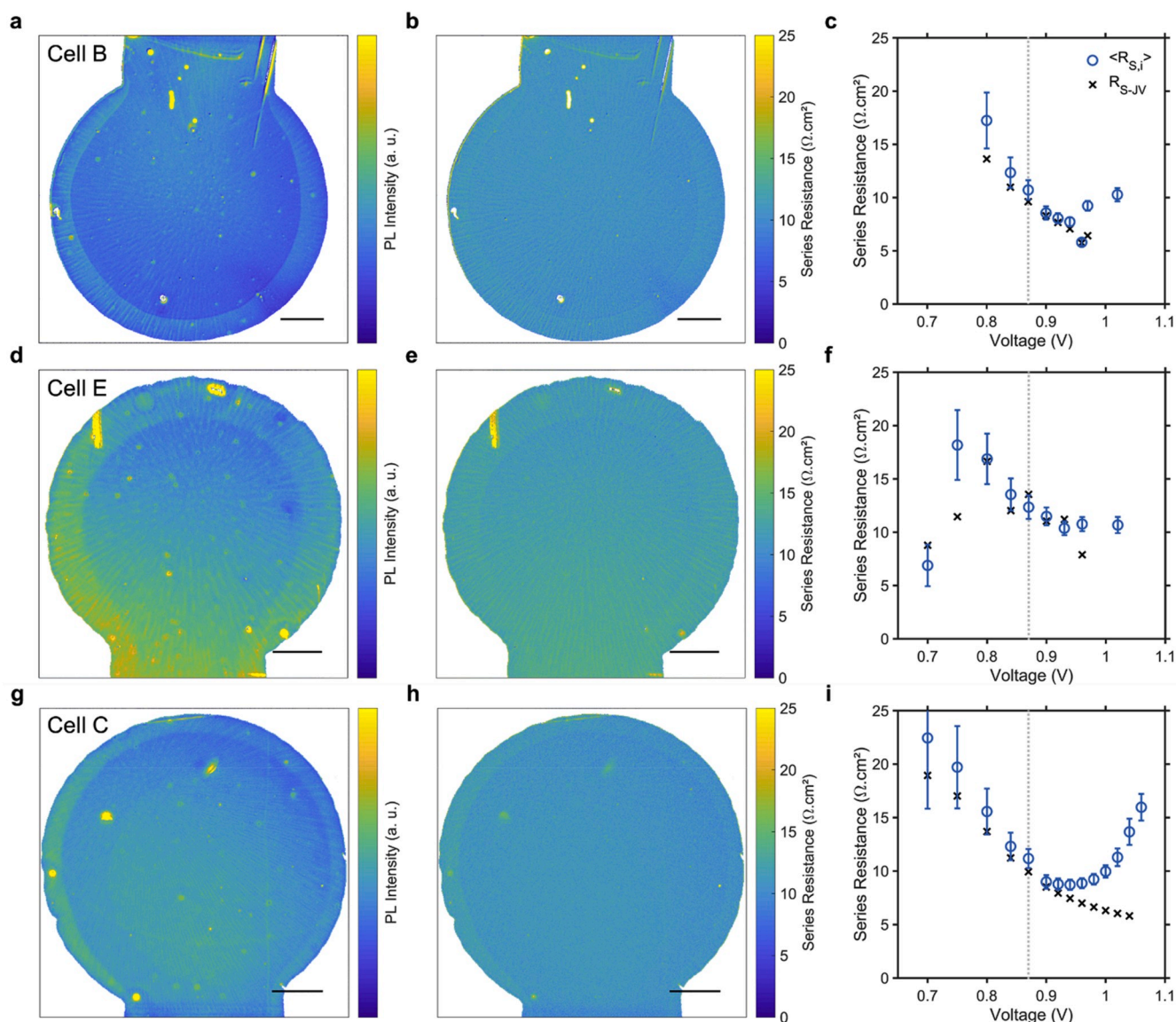


Fig. 4. Photoluminescence intensity (left, a,d,g) and series resistance $R_{S,i}$ maps (middle, b,e,h) measured at V_{MPP} for a selection of cells with scale bars representing 1 mm. (Right, c,f,i) plots of the mean local series resistance determined from sine fits $\langle R_{S,i} \rangle$ and the global resistance calculated using the MLM method $R_{S,JV}$ for a range of voltages; circles and crosses, respectively. A dotted line indicates V_{MPP} for each cell. From top to bottom the cells are B, E and C. In the maps white denotes pixels outside of the device or pixels that exhibit a negative resistance. Since the cells are circular, for ease of analysis the $\langle R_{S,i} \rangle$ was determined from a large square ($\sim 3.5 \times 3.5 \text{ mm}^2$) in the centre of the devices.

precursors during fabrication, local defects causing de-wetting after spin coating of a film and in the case of small circles, regions of high dopant concentration [28].

For the inverted cells, a large circular feature can be observed which matches the size of the aperture masked used during current-voltage analysis with the solar simulator performed prior to the PL study presented here, (Figs. S10–S12). The area exposed to light shows reduced series resistance which is supported by a slight improvement in J_{SC} with light soaking.

In the series resistance maps, for most of the cells presented here, there is a region of high series resistance at the perimeter of the Au back contact, although the width varies between samples. To assist in this analysis we will refer to electroluminescence intensity maps provided in the supplementary information. For these measurements, we simply applied a set current of 14–20 mA/cm² (close to J_{SC}) and waited for the voltage to stabilise before measuring a PL intensity map. Comparison of EL and PL maps for a cell can provide useful qualitative insights for specific features of the cell [26,31]. For instance, regions of high series resistance typically limit charge extraction in PL and exhibit a high PL intensity while preventing charge injection in electroluminescence and exhibit a low EL intensity. In this region there is generally a reduced EL but enhanced PL signal, confirming a higher series resistance. This feature most likely reflects a higher sheet resistance in the Au contact due to edge effects and/or reduced thickness due to a slight shadowing from the mask during the Au deposition [39,40].

At this point it is worth noting an artefact of the analysis, in which areas of particularly high series resistance may exhibit a negative resistance, indicated by white pixels within the cell. This occurs in regions where the PL intensity is high but shows a slight reduction with voltage; however, it is easy to distinguish these points as they are typically surrounded by or at least adjacent to pixels with high resistance.

It is insightful to compare the mean series resistance from the PL analysis $\langle R_{S,i} \rangle$ with the corresponding values from the MLM analysis $R_{S,JV}$. The voltage dependence of the series resistances is shown in Fig. 4 and the supplementary information for each cell. There is a general reduction in the series resistance which has been observed in PSCs and silicon solar cells [31,37] while the opposite trend is true for CdTe based devices [12]. From the three plots in Fig. 4, it is clear that there is generally good agreement around $V_{Term} \sim -V_{MPP}$, however, away from these voltages and there is an increase in the standard deviation of $R_{S,i}$. A key reason for the discrepancy is the wide voltage range we have chosen 0.2–0.35 V around V_{MPP} , greatly exceeding the window of only 0.1 V in previous works [31]. The use of an extended voltage range was intentional as it provides insights into the limitations of series resistance mapping of perovskite solar cells.

At lower voltages, below 0.7 V, the local series resistance analysis begins to fail because the overall PL intensity approaches the background level and the low signal-to-noise ratio, results in a large standard deviation with many pixels exhibiting a non-physical negative resistance which are subsequently disregarded. At voltages greater than V_{MPP} , approaching the open circuit voltage V_{OC} the situation is more complicated. In some cells, there is an unexpected reduction in the variation in the PL intensity with V_{Term} , this would be reflected in Fig. 3 as a smaller offset in dV_i at different V_{Term} values. Resulting in an increase in $R_{S,i}$ as can be seen in Fig. 4i. In more drastic cases, at voltages within 100 mV of V_{OC} , a slight reduction in the PL intensity at some pixels results in pixels exhibiting negative resistances and are similarly discarded. However, the $R_{S,JV}$ values are not affected, and cell and subsequent EL measurements reveal that the cell is not irreversibly degraded. These results suggest that although a steady state condition is required for meaningful measurements, it alone is not the sole requirement.

In Fig. 5 we compare the resistances at $\sim V_{MPP}$ for each cell. For two cells, (D and G) the $R_{S,i}$ analysis appears to have failed, with large variations between the local and global resistances across the entire voltage range with a discrepancy in excess of 10 $\Omega \text{ cm}^2$ at V_{MPP} , shown in supplementary information. The ability to easily identify problematic

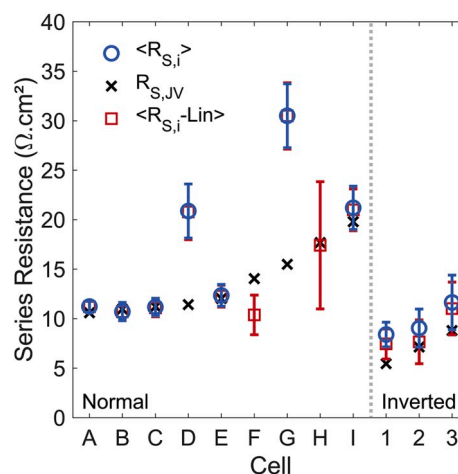


Fig. 5. Comparison of the mean local series resistances $\langle R_{S,i} \rangle$ and $\langle R_{S,i-Lin} \rangle$ with the global series resistance ascertained $R_{S,JV}$, at V_{MPP} for each cell. Cells are arranged with increasing $R_{S,JV}$ moving from left to right for the two set of cells, normal and inverted structures. For cells F and H, a stability criteria was used at each light intensity as opposed to modulation, so $\langle R_{S,i} \rangle$ was not determined.

results is advantageous for routine analysis. For the other 10 samples there is very good general agreement and we note there was no obvious trend between the discrepancies in the mean of the local and global series resistances or any other photovoltaic parameters. The mean local and global series resistances of the batch of normal structured cells in this work are 13.4 ± 2 (excluding D and G) and $13.7 \pm 3.3 \Omega \text{ cm}^2$, which are notably higher than the $\sim 6 \Omega \text{ cm}^2$ reported by other for mixed cation PSCs admittedly with slightly higher efficiencies [31]. However, the inverted cells enjoy lower resistances of 9.7 (local) and $7.1 \Omega \text{ cm}^2$ (global).

4. Discussion

Firstly, it is important to comment on the validity of the series resistance mapping method developed in this work before comparing it to existing approaches. So far we have demonstrated that the features in the $R_{S,i}$ maps reflect those present in both the PL and EL maps and we have shown good agreement between the global and mean local resistance. A crucial assumption has been that the light modulation provides a suitable modulation in the PL intensity. Since we use the approximation $J_L = J_{SC}$, there is an inherent calibration of the intensity for the analysis i.e. if a higher or lower set of illumination intensities are used, the analysis will still proceed as expected and provide meaningful series resistance maps. To ensure the validity of the PL modulation, for cells F and H, the fixed rate of light modulation was replaced with the stability criteria at each light intensity. The settling interval at 1 Sun was set to 60 s but for subsequent light intensities at the same voltage this interval was reduced to only 5 s to prevent excess measurement times. Repeated measurements on these cells lead to some reversible changes in the PL intensity (that recovered after a day) and observed irreversible changes which increased the disparity between the two resistances. Instead of comparing the two methods directly as intended, we rely on the similarity in the results between the cells measured using the different approaches.

Taking the above remarks into consideration, we compare our series resistance mapping to published methods employed for silicon and thin film photovoltaics and perovskite solar cells [7,13,15–19,31,32,38,41]. The various approaches can be split into two categories, between whether or not they consider the voltage dependence of the series resistance. Unique to our approach is the capability to produce maps at each potential-step with pre-existing methods providing about only half the number of maps per-step over a more limited voltage range [12,31].

Series resistance mapping of perovskite solar cells has the added complication of requiring the current to be stabilised prior to analysis, which can significantly increase the total time necessary for measurement. Since the time required to wait for stabilisation varies between cells, it difficult to compare absolute measurement times with the only reported approach used on PSCs by Walter et al. [31] However, it is worth noting that our approach requires a quarter of the number of occurrences for stabilisation, since their methods requires essentially four dynamic JV curves. When using the IMPL-Map approach on the normal structure cells, our analysis time per potential-step, was 1.3 min and with a median of 17 potential-steps, the average measurement time was ~23 min. Since the minimal number of potential-steps for determining a series resistance map is 3 (including 1 calibration and 2 comparison voltages, ideally around V_{MPP}) the measurement time could potentially be reduced to ~4 min. For the inverted cells, which exhibited less hysteresis and stabilised much faster, the measurement time could be ~3 min.

5. Conclusion

A new camera-based luminescence method for mapping the series resistance of PSCs has been developed. We demonstrate that once a steady state condition has been achieved, the light intensity can be modulated, to reduce the measurement time while improving the number of maps that can be produced per voltage step. The applicability of our method has been demonstrated with a batch of typical research cells with high series resistance $13.7 \pm 3.3 \Omega \text{ cm}^2$, significant hysteresis and moderate PCEs of ~16%. The magnitude of the local series resistances has been shown to agree well with the series resistances determine using the MLM method, which offers an inherent validation that has proven useful in identifying the fallacious results of two cells. The results presented here show clear evidence that the performance of the devices is affected by spatially inhomogeneities on a macroscale. Furthermore, our technique is robust can be readily be applied as a routine analysis tool for research cells and uses simple infrastructure that can be readily up-scaled to analyse large area cells or modules.

6. Experimental methods

Two devices architectures, n-i-p and p-i-n, were employed in this study. The n-i-p or normal structure is comprised of Glass|FTO|c-TiO₂|mp-TiO₂||Rb_{0.05}Cs_{0.05}FA_{0.8}MA_{0.07}PbI_{2.57}Br_{0.4}|Spiro|au. The p-i-n or inverted structure consists of Glass|FTO|PEDOT:PSS|PTAA|Rb_{0.05}Cs_{0.05}FA_{0.8}MA_{0.07}PbI_{2.57}Br_{0.4}|PCBM|BCP|Au.

6.1. Materials

All materials were purchased from either Alfa Aesar or Sigma-Aldrich and used without further purification unless otherwise specified. Methylammonium iodide (MAI), formamidinium iodide (FAI), methylammonium bromide (MABr) were purchased from Greatcell Solar Ltd. 2,2',7,7'-Tetrakis [N,N-di(4-methoxyphenyl)amino]-9,9'-spirobifluorene (spiro-OMeTAD) was purchased from Luminescence Technology Corp. Glass substrates with a conductive layer of fluorine-doped tin oxide (FTO) of $8 \Omega \text{ sq}^{-1}$ sheet resistance were purchased from Zhuhai Kaivo Optoelectronic Tech. Corp.

6.2. Preparation of the perovskite precursor solution and spiro-OMeTAD solution

The perovskite precursor solution was prepared in a N₂-filled glovebox by mixing 1.1 M PbI₂, 0.2 M PbBr₂, 0.09 M MABr, 1.05 M FAI, 0.0063 M CsI and 0.0063 M RbI precursor solutions in a mixture of anhydrous N,N-dimethylformamide (DMF) and dimethyl sulfoxide (DMSO) in 4:1 vol ratio. The final composition of the perovskite solution was Rb_{0.05}Cs_{0.05}FA_{0.8}MA_{0.07}PbI_{2.57}Br_{0.4}. The perovskite solution was

stirred overnight until fully dissolved prior to spin-coating. The spiro-OMeTAD solution was prepared by dissolving 67.2 mM spiro-OMeTAD in chlorobenzene and then 230 mM tBP and 27.2 mM LiTFSI (500 mg mL⁻¹ in acetonitrile).

6.3. n-i-p solar cell fabrication

The FTO-coated glass substrates were laser patterned and cleaned in ultra-sonication bath with 2% (volume ratio) Hellmanex solution, water and then ethanol (each for 15 min sequentially). A 15 nm compact TiO₂ layer was deposited at 500 °C with an automatic spray pyrolysis system using a titanium-diisopropoxide bis(acetylacetonate) solution in isopropanol (1:19, v/v). The substrates were sintered for 10 min at 500 °C afterwards and cooled to room temperature. The substrates were then cut to pieces with size of 2.5 cm × 2.5 cm and cleaned with UV plasma cleaner for 10 min. The mesoporous TiO₂ layer was prepared by spin-coating of diluted TiO₂ paste (NR-30: ethanol = 1:6, mass ratio) at 4000 rpm for 20 s with a ramping speed of 2000 rpm s⁻¹. Then the substrates were sintered at 500 °C for 30 min and a 150 nm thick meso-TiO₂ layer was formed. The substrates were treated again with a UV-plasma cleaner for 10 min and then transferred to a N₂-filled glovebox for perovskite deposition. Then 35 μL cm⁻² of perovskite precursor solution was spread onto the substrates and spin-coated with a two-step program including a first step at 1000 rpm for 10 s with a ramping speed of 1000 rpm s⁻¹ and 4000 rpm for 30 s with a ramping speed of 2000 rpm s⁻¹. Chlorobenzene, 110 μL was poured onto the substrate 10 s prior to the end of the second step. The substrates were then annealed at 100 °C for 1 h. After cooling, 35 μL cm⁻² of spiro-OMeTAD solution was deposited on the perovskite layer and spin coated at 3000 rpm for 30 s.

6.4. p-i-n solar cell fabrication

A Poly(3,4-ethylenedioxythiophene) polystyrene sulfonate (PEDOT:PSS) (Al 4083) solution was prepared by diluting the purchased PEDOT:PSS (Heraeus CLEVIOS) with methanol in a 1:4 PEDOT:PSS:MeOH ratio. We spin coated this solution statically in an air atmosphere at 3000 rpm with a ramp rate of 1000 rpm s⁻¹, and annealed the substrate at 100 °C for 10 min in air. A Poly[bis(4-phenyl) (2,4,6-trimethylphenyl)amine] (PTAA) precursor solution was prepared by dissolving a 1.5 mg ml⁻¹ PTAA (Xi'an Polymer) in a 1:1 anhydrous chloroform (CF): chlorobenzene (CB). We spin coated this solution dynamically in a nitrogen-filled glovebox at 2000 rpm, and annealed the substrate at 150 °C for 10 min in air. To fabricate the p-i-n solar cells, we employed the identical Rb_{0.05}Cs_{0.05}FA_{0.8}MA_{0.07}PbI_{2.57}Br_{0.4} perovskite solution described above. We spin coated this solution statically in a nitrogen-filled glovebox at 6000 rpm with a ramp rate of 1000 rpm s⁻¹ for 30 s. Ethyl acetate, 100 μL was poured onto the substrate 5 s prior to the end of the spin coating. We then annealed the substrate at 100 °C for 1 h. A Phenyl-C61-butyric acid methyl ester (PC₆₁BM) precursor solution was prepared by dissolving a 15 mg ml⁻¹ PC₆₁BM (99%, solenne) in a 9:1 anhydrous chloroform (CF): chlorobenzene (CB) (Sigma). We spin coated this solution dynamically in a nitrogen-filled glovebox at 2500 rpm, and annealed the substrate at 100 °C for 10 min. A Bathocuproine (BCP) precursor solution was prepared by dissolving a 0.5 mg ml⁻¹ BCP (>99.5%, sigma) in anhydrous isopropanol (IPA). We spin coated this solution dynamically in a nitrogen-filled glovebox at 6000 rpm.

6.5. Au deposition

In the last step, 80 nm of gold electrode was thermally evaporated through a shadow mask. To ensure minimal degradation occurred during the measurement, the devices were left in the dry-box for 3 h and then encapsulated in a N₂-filled glovebox.

6.6. *J-V curve*

The photovoltaic performance of each solar cell was measured using a bio logic potentiostat and an Abet Technologies Sun 3000 class AAA with an AM 1.5G spectrum at 100 mW cm^{-2} . The irradiation area was defined with a non-reflective metal aperture of 0.16 cm^2 . The *J-V* measurement was obtained in both reverse (1.2 to -0.1 V) and forward (-0.1 – 1.2 V) scan directions in 10 mV steps with settling times of 100 ms (0.1 V s^{-1}). The devices were stabilised for 3 s under illumination prior to scanning. For the inverted cell, the scan speed was 0.3 V s^{-1} , after 2 min of light soaking. The stabilised power output was obtained by holding the devices at the potential corresponding to the maximum powerpoint of the *J-V* curve in reverse scan for 60 s . These results are provided in the supplementary information.

6.7. *Dynamic J-V curve*

During dynamic *IV* curves the cells were illuminated by an LED array with peak wavelength in 447 nm , powered by a Keithley 2220. The intensity of light was measured with a silicon solar cell and then slightly corrected to ensure the same J_{SC} for a perovskite cell as measured in a solar simulator. A series of optics were used to ensure the light source enjoyed a spatial variation intensity of less than 10% over an area of $1 \text{ cm} \times 1 \text{ cm}$, although the cells were almost circular with a diameter of 6 mm .

Dynamic *IV* scans were performed using a Keithley 2400 by starting at $V = -0.5 \text{ V}$ and incrementally raising the voltage to open circuit or slightly beyond. At each voltage the current was monitored and once it had stabilised, the rate of change was below a threshold from 1 to $3.5 \times 10^{-6} \text{ A/s}$ and/or $0.1\%/s$, determined by the gradient of a linear regression of the current (or voltage at V_{OC}) for data of a settling interval of 20 (inverted cells) and 60 s (normal), the light intensity was modulated by DC variation of the Keithley 2220. To prevent local minima/maxima in values from falsely triggering the stability condition, an additional criteria was imposed that the sign of gradient had to remain constant over the settling interval. Throughout this study we found that the PL analysis was highly sensitive to pre-conditioning and for dynamics *IV* scans, samples were only measured once per day.

The rate of the modulation, number of points per period and number of periods were varied to investigate the effects of these parameters, however, the inherent variation between cells proved to dominate the results. For samples F and H rather than using the fixed modulation $\sim 0.2 \text{ Hz}$ we used the aforementioned stability criteria at each light intensity, however, once stability was achieved at 1 Sun the settling interval was reduced to only 5 s . This measurement scheme was used to provide series resistance maps without the use modulation in order to draw a comparisons. The results between the two methods proved to be similar except stabilising at each change in light intensity significantly increased the measurement. For all samples, the current measured at J_{SC} was used to determine the photocurrent J_L at each light intensity during the modulation for each cell. A list of the measurement parameters is provided in supplementary information.

Electroluminescence was performed by applying 14 – 20 mA/cm^2 to the solar cell and waiting for stability using the criteria above with a settling interval of 20 s using the aforementioned setup. Longer stability times lead to degradation of the EL intensity.

The photo- and electroluminescence was captured using a D610 with a VR Micro-NIKKOR 105 mm f/2.8G lens and the inherent IR filter prior to the sensor removed. A band pass filter $775/50 \text{ nm}$ was placed between the sample and camera lens to ensure only the luminescence from the perovskite was captured. The photos were captured using an ISO of 100 , an aperture of $f/4.5$ – 5 and a shutter speeds of about 0.25 s but was varied to prevent images from saturating. The pixel size is $\sim 10 \times 10 \mu\text{m}^2$. All PL images were background corrected by subtracting the PL images measured at -0.5 V , at the same light intensity [7,13–19]. The two Keithleys and the camera were controlled using a custom LabVIEW

program and the data post-processed using a MATLAB script.

Declaration of competing interest

The authors declare that they have no known competing financial interests or personal relationships that could have appeared to influence the work reported in this paper.

CRediT authorship contribution statement

Kevin J. Rietwyk: Investigation, Conceptualization, Methodology, Data curation, Writing - original draft. **Boer Tan:** Validation, Resources, Writing - review & editing. **Adam Surmiak:** Methodology, Resources. **Jianfeng Lu:** Resources, Writing - review & editing. **David P. McMeekin:** Resources. **Sonia R. Raga:** Supervision, Writing - review & editing. **Noel Duffy:** Project administration, Supervision, Writing - review & editing. **Udo Bach:** Funding acquisition, Project administration, Supervision.

Acknowledgement

The authors are grateful for the financial support by the Australian Research Council (ARC) Centre of Excellence in Exciton Science (ACEX: CE170100026). D.P.M. acknowledges financial support from the Australian Centre for Advanced Photovoltaics (ACAP).

Appendix A. Supplementary data

Supplementary data to this article can be found online at <https://doi.org/10.1016/j.nanoen.2020.104755>.

References

- [1] NREL, Best research-cell efficiencies chart - revised 02/08/2019. <https://www.nrel.gov/pv/assets/pdfs/pv-efficiency-chart.20181221.pdf>.
- [2] A. Kojima, K. Teshima, Y. Shirai, T. Miyasaka, Organometal halide perovskites as visible-light sensitizers for photovoltaic cells, *J. Am. Chem. Soc.* **131** (2009) 6050–6051.
- [3] Y. Rong, et al., Challenges for commercializing perovskite solar cells, *Science* **361** (2018) eaat8235.
- [4] F. Wang, et al., Materials toward the upscaling of perovskite solar cells: progress, challenges, and strategies, *Adv. Funct. Mater.* **28** (2018), 1803753.
- [5] Z. Li, et al., Scalable fabrication of perovskite solar cells, *Nat. Rev. Mater.* **3** (2018) 18017.
- [6] M.A. Green, et al., Solar cell efficiency tables (version 54), *Prog. Photovoltaics Res. Appl.* **27** (2019) 565–575.
- [7] J. Haunschild, et al., Quality control of as-cut multicrystalline silicon wafers using photoluminescence imaging for solar cell production, *Sol. Energy Mater. Sol. Cells* **94** (2010) 2007–2012.
- [8] R. Bhoopathy, O. Kunz, M. Juhl, T. Trupke, Z. Hameiri, Outdoor photoluminescence imaging of photovoltaic modules with sunlight excitation, *Prog. Photovoltaics Res. Appl.* **26** (2018) 69–73.
- [9] Y. Zhu, M.K. Juhl, T. Trupke, Z. Hameiri, Photoluminescence imaging of silicon wafers and solar cells with spatially inhomogeneous illumination, *IEEE J. Photovolt.* **7** (2017) 1087–1091.
- [10] U. Rau, et al., Photocurrent collection efficiency mapping of a silicon solar cell by a differential luminescence imaging technique, *Appl. Phys. Lett.* **105** (2014), 163507.
- [11] T. Trupke, R.A. Bardos, M.C. Schubert, W. Warta, Photoluminescence imaging of silicon wafers, *Appl. Phys. Lett.* **89** (2006), 044107.
- [12] A. Ren, et al., A luminescence-based interpolation method for series resistance imaging in thin film solar cells, *Jpn. J. Appl. Phys.* **58** (2019), 050908.
- [13] H. Kampwerth, T. Trupke, J.W. Weber, Y. Augarten, Advanced luminescence based effective series resistance imaging of silicon solar cells, *Appl. Phys. Lett.* **93** (2008), 202102.
- [14] Y. Augarten, et al., Calculation of quantitative shunt values using photoluminescence imaging: calculation of quantitative shunt values using PL imaging, *Prog. Photovoltaics Res. Appl.* (2012), <https://doi.org/10.1002/pip.2180>.
- [15] M. Glatthaar, et al., Evaluating luminescence based voltage images of silicon solar cells, *J. Appl. Phys.* **108** (2010), 014501.
- [16] O. Breitenstein, et al., Quantitative evaluation of electroluminescence images of solar cells, *Phys. Status Solidi RRL - Rapid Res. Lett.* **4** (2010) 7–9.
- [17] M. Seeland, C. Kästner, H. Hoppe, Quantitative evaluation of inhomogeneous device operation in thin film solar cells by luminescence imaging, *Appl. Phys. Lett.* **107** (2015), 073302.

- [18] P. Song, J. Liu, M. Oliullah, Y. Wang, Series resistance imaging of silicon solar cells by lock-in photoluminescence: series resistance imaging of silicon solar cells by lock-in PL, *Phys. Status Solidi RRL - Rapid Res. Lett.* 11 (2017), 1700153.
- [19] H. Höfler, J. Haunschild, R. Zeidler, S. Rein, Statistical evaluation of a luminescence-based method for imaging the series resistance of solar cells, *Energy Procedia* 27 (2012) 253–258.
- [20] S. Mastroianni, et al., Analysing the effect of crystal size and structure in highly efficient $\text{CH}_3\text{NH}_3\text{PbI}_3$ perovskite solar cells by spatially resolved photo- and electroluminescence imaging, *Nanoscale* 7 (2015) 19653–19662.
- [21] R.J. Stoddard, et al., Enhancing defect tolerance and phase stability of high-Bandgap perovskites via Guanidinium alloying, *ACS Energy Lett* 3 (2018) 1261–1268.
- [22] R.J. Stoddard, F.T. Eickemeyer, J.K. Katahara, H.W. Hillhouse, Correlation between photoluminescence and carrier transport and a simple in situ passivation method for high-Bandgap hybrid perovskites, *J. Phys. Chem. Lett.* 8 (2017) 3289–3298.
- [23] I.L. Braly, R.J. Stoddard, A. Rajagopal, A.K.-Y. Jen, H.W. Hillhouse, Photoluminescence and photoconductivity to assess maximum open-circuit voltage and carrier transport in hybrid perovskites and other photovoltaic materials, *J. Phys. Chem. Lett.* 9 (2018) 3779–3792.
- [24] M. Stolterfoht, et al., Visualization and suppression of interfacial recombination for high-efficiency large-area pin perovskite solar cells, *Nat. Energy* 3 (2018) 847–854.
- [25] I.L. Braly, H.W. Hillhouse, Optoelectronic quality and stability of hybrid perovskites from MAPbI_3 to MAPbI_2Br using composition spread libraries, *J. Phys. Chem. C* 120 (2016) 893–902.
- [26] A.M. Soufiani, et al., Lessons learnt from spatially resolved electro- and photoluminescence imaging: interfacial delamination in $\text{CH}_3\text{NH}_3\text{PbI}_3$ planar perovskite solar cells upon illumination, *Adv. Energy Mater.* 7 (2017), 1602111.
- [27] A.M. Soufiani, et al., Electro- and photoluminescence imaging as fast screening technique of the layer uniformity and device degradation in planar perovskite solar cells, *J. Appl. Phys.* 120 (2016), 035702.
- [28] H. Shen, et al., Improved reproducibility for perovskite solar cells with 1 cm^2 active area by a modified two-step process, *ACS Appl. Mater. Interfaces* 9 (2017) 5974–5981.
- [29] A.M. Soufiani, J. Kim, A. Ho-Baillie, M. Green, Z. Hameiri, Luminescence imaging characterization of perovskite solar cells: a note on the analysis and reporting the results, *Adv. Energy Mater.* 8 (2018), 1702256.
- [30] B. Chen, et al., Imaging spatial variations of optical Bandgaps in perovskite solar cells, *Adv. Energy Mater.* (2018), 1802790, <https://doi.org/10.1002/aenm.201802790>.
- [31] D. Walter, et al., On the use of luminescence intensity images for quantified characterization of perovskite solar cells: spatial distribution of series resistance, *Adv. Energy Mater.* 8 (2018) 1701522.
- [32] Y. Wu, et al., On the origin of hysteresis in perovskite solar cells, *Adv. Funct. Mater.* 26 (2016) 6807–6813.
- [33] J. Krüger, R. Plass, M. Grätzel, P.J. Cameron, L.M. Peter, Charge transport and back reaction in solid-state dye-sensitized solar cells: a study using intensity-modulated photovoltage and photocurrent spectroscopy, *J. Phys. Chem. B* 107 (2003) 7536–7539.
- [34] A. Pockett, et al., Characterization of planar lead halide perovskite solar cells by impedance spectroscopy, open-circuit photovoltage decay, and intensity-modulated photovoltage/photocurrent spectroscopy, *J. Phys. Chem. C* 119 (2015) 3456–3465.
- [35] A. Dymshits, A. Rotem, L. Etgar, High voltage in hole conductor free organo metal halide perovskite solar cells, *J. Mater. Chem.* 2 (2014) 20776–20781.
- [36] M. Wolf, H. Rauschenbach, Series resistance effects on solar cell measurements, *Adv. Energy Convers.* 3 (1963) 455–479.
- [37] K.C. Fong, K.R. McIntosh, A.W. Blakers, Accurate series resistance measurement of solar cells: accurate series resistance measurement of solar cells, *Prog. Photovoltaics Res. Appl.* (2011), <https://doi.org/10.1002/pip.1216> n/a-n/a.
- [38] M. Glatthaar, et al., Spatially resolved determination of dark saturation current and series resistance of silicon solar cells, *Phys. Status Solidi RRL - Rapid Res. Lett.* 4 (2010) 13–15.
- [39] S.K. Yao, Theoretical model of thin-film deposition profile with shadow effect, *J. Appl. Phys.* 50 (1979) 3390–3395.
- [40] S. Bahamondes, S. Donoso, A. Ibañez-Landeta, M. Flores, R. Henriquez, Resistivity and Hall voltage in gold thin films deposited on mica at room temperature, *Appl. Surf. Sci.* 332 (2015) 694–698.
- [41] M. Kasemann, et al., Contactless qualitative series resistance imaging on solar cells, *IEEE J. Photovolt.* 2 (2012) 181–183.